Control-Oriented Physics-Based Modeling and Observer Design for State-of-Charge Estimation of Lithium-Ion Cells for High Current Applications

Anirudh Nath[ID], *Member, IEEE*, Rohit Mehta[ID], Raghvendra Gupta[ID], Supreet Singh Bahga, Amit Gupta, and Shubhendu Bhasin[ID], *Member, IEEE*

Abstract—This article proposes a physics-based control-oriented model and observer design for the state-of-charge (SoC) estimation of lithium-ion cells for applications involving high magnitude fluctuating current profiles. The physics-based single-particle model (SPM) provides enhanced accuracy due to the inclusion of electrolyte dynamics and addresses the issue of nonobservability associated with it. The computationally efficient physics-based model is utilized to design a robust observer-based SoC estimator in the framework of linear matrix inequality to guarantee fast convergence despite parametric uncertainty in the state and output equations, and unknown initial conditions. The observer performance is validated using FTP75 and US06 dynamic tests at different temperatures, and the results are compared with the standard unscented Kalman filter (UKF). The mean SoC estimation error and the integral square error of the estimated SoC for the proposed observer are at least one order of magnitude smaller than that of UKF. Furthermore, robustness to ±30% parametric uncertainty, measurement noise, and unknown initial conditions is demonstrated through Monte Carlo simulations at different temperatures.

Index Terms—Linear matrix inequality (LMI), lithium-ion cell, observer, single-particle model (SPM), state of charge (SoC).

I. INTRODUCTION

IN THE recent decade, significant interest has developed in the research community toward the application of lithium-ion batteries for powering electric vehicles (EVs). Lithium-ion batteries have become an efficient and reliable energy storage system due to their high energy-to-weight ratio, low self-discharge, and negligible memory effect in comparison to other battery chemistries [1]. Safe and reliable operation of batteries demands continuous monitoring of their internal states, including remaining capacity and temperature, to prevent them from being subjected to adverse conditions. This task is performed by a battery management system (BMS) that monitors states, such as the state of charge (SoC), state of health (SoH), and temperature, thereby preventing the batteries from being subjected to overcharge, overdischarge, and thermal runaway [2].

The SoC is a crucial parameter that provides a measure of the remaining charge capacity in a cell under operation. Since the SoC cannot be measured directly, various techniques have been formulated and implemented for its estimation [3]. One of the simplest techniques is the ampere-hour counting method that involves discrete integration of current over time. However, being an open-loop method, it requires precise information of the initial SoC, which is difficult to obtain in a practical scenario. Furthermore, it may suffer from error accumulation due to integration operation over large time steps [4]. Another technique based on open-circuit potential (OCP) measurement is not suitable for online observation as this requires a long relaxation time for the determination of SoC at any instant during operation. The data-based learning techniques, including neural network and fuzzy logic, require extensive training data specific to the battery under consideration and may be difficult to obtain for individual cells. These techniques also suffer from issues of high computational cost, overfitting, and lack of information about the internal states of the battery [3]. SoC estimation techniques based on the equivalent circuit model (ECM) can lead to erroneous SoC estimation since the ECM is essentially an empirical relationship between the current and terminal voltage [2], [4], [5]. On the other hand, physics-based models consider species and charge transport phenomena within cells and can provide an accurate prediction of battery states. In the category of physics-based model approaches, the pseudo-2-D (P2D) model based on the electrochemistry of the lithium-ion cell is well-established [6]. However, the P2D model is computationally expensive as it involves solving coupled nonlinear differential-algebraic equations (DAEs) and, thus, has not been practically realizable for real-time SoC estimation, particularly for low-cost BMS [7]. Various simplifications have been considered to overcome this limitation. One such approach is the single-particle model (SPM) [8], which assumes a uniform current density in the electrodes and ignores electrolyte dynamics.

Anirudh Nath and Shubhendu Bhasin are with the Department of Electrical Engineering, IIT Delhi, New Delhi 110016, India (e-mail: anirudhnath@ee.iitd.ac.in; sbhasin@ee.iitd.ac.in).

Rohit Mehta, Raghvendra Gupta, Supreet Singh Bahga, and Amit Gupta are with the Department of Mechanical Engineering, IIT Delhi, New Delhi 110016, India (e-mail: rohit0149@gmail.com; raghvendrag6@gmail.com; bahga@mech.iitd.ac.in; agupta@mech.iitd.ac.in).

The lithium transport in each electrode is solved for a single-spherical particle [9]. Various works on SoC estimation have incorporated this model [10]–[12]. However, ignoring electrolyte dynamics limits the applicability of the SPM to low C-rates ($<C/2$) only [13]. Another reduced-order model, namely, the equivalent-hydraulic model (EHM), uses two tanks to represent the surface and internal storage of lithium within the electrode particles [14], [15]. The EHM is an analogous but approximate representation of diffusion physics and cannot account for the effect of particle diffusivity and the spatial concentration gradient existing within electrode particles. Hence, SPM and EHM are not suitable for the SoC estimation algorithms in EVs where cells routinely experience C-rates up to 10 C under extreme scenarios.

Several mathematical models have also been proposed to improve the SPM by incorporating electrolyte dynamics. Most of results have attempted to model the electrolyte potential drop in the cell [16]–[20]. The model developed by Prada *et al.* [16] has found application in several estimation algorithms [20]. While some of these works have ignored the electrolyte dynamics [21]–[23], others have considered a polynomial model to obtain the lithium concentration in the electrolyte [17], [18], [24]. Recently, SPM incorporating electrolyte dynamics was proposed, which considered the effect of spatial variations of the overpotential and the OCP in the cell voltage [13]. The proposed model was able to predict cell voltage within 2% accuracy to that of P2D for discharge and charge rates up to a 5-C rate.

Previous works on modeling the dynamics of lithium-ion cells have employed either domain discretization techniques (DDTs) [10]–[12], [23] [such as the finite-volume method (FVM) or finite-difference method (FDM)] or fourth-degree polynomial model [25]–[28] to obtain the solution of the electrode diffusion equation. While DDT requires many nodes to obtain a converged solution, the polynomial models can result in significant error under highly fluctuating currents. In addition, several analytical solutions for the diffusion equation exist in the literature [17], [29]. The model of Guo and White [29] has been shown to accurately represent the diffusion dynamics with relatively lower computational cost than DDTs. [13]. The linearized modeling in [13] while being computationally efficient is amenable for control and estimation and, therefore, motivated the proposed work.

Furthermore, considering the dynamics of both the positive and negative electrodes independently leads to the issue of nonobservability [23]. A single-electrode representation and an approximated linear relation between the two electrodes' surface concentration have been considered in [10], [12], [18], and [23] to overcome this issue though resulting in an inaccurate prediction of the surface concentration. In [30], an interconnected cascaded observer structure is used for estimating the lithium-ion surface concentrations in both electrodes. The charge and species conservation equations are solved using FDM, thereby increasing the dimension of the state-space model and, hence, the complexity. A temperature sensor-based approach was adopted in [31] to circumvent nonobservability in SPM, albeit at a higher cost due to the inclusion of this sensor.

Recent works that incorporate the electrolyte dynamics use an open-loop observer to estimate the electrolyte states [17], [18], [24], [32], which can lead to erroneous SoC estimates due to the absence of self-correcting terms and unavailability of information about the internal states [3]. The efficacy of these algorithms is further reduced in the presence of parametric uncertainty and modeling inaccuracies.

Various variants of the Kalman filter (KF)-based SoC estimation techniques have been extensively studied in the literature. The ability of the stochastic filter-based approaches, such as the extended KF (EKF) [33]–[35], unscented KF (UKF) [3], [36], [37], and particle filter (PF) [38], to deal with inherent system nonlinearity put these algorithms in the forefront. Recently, EKF has been applied to a control-oriented SPM (COSPM) to estimate the internal states [39]. However, these algorithms have limitations in terms of complex matrix operations and require characterization of the system uncertainty, which can be difficult to obtain in practice for a particular cell chemistry and application [2], [3].

Deterministic observer-based SoC algorithms have also recently gained widespread interest. The H_∞ filter [5], [40] and sliding mode observers (SMOs) [2], [41] are the two most common techniques that have been explored for SoC estimation. Like their stochastic counterparts, the H_∞ filters incur a high computational burden for their implementation [2]. On the other hand, SMOs have been known to suffer from chattering issues [42] and often require the use of filters that induce additional lags and increase the implementation complexity [2], [43]. In [12], a combination of surface concentration observer with an adaptive observer was proposed. The parameter adaptation in the adaptive observer demands online computation of the uncertain parameters, thereby increasing the computational burden. Another SPM-based observer was proposed in [28], which dealt with output uncertainty in the model through recursive least squares to identify uncertain parameters. However, the structural uncertainty pertaining to the state equation evolving out of varying conditions, such as temperature, was not addressed. This discussion reveals that, to obtain a highly reliable real-time SoC estimate, one needs a high-fidelity mathematical model of the lithium-ion cell with a robust state estimation framework to estimate the internal states.

In this article, we propose a COSPM with the combined dynamics of the electrodes and the electrolyte, and is based on the reduced-order model proposed in [13]. The COSPM incorporates the effect of the spatial variation in ionic potential, overpotential, and OCP on the cell voltage, thereby leading to a better estimation of the cell voltage, as demonstrated in this article. A semianalytical solution for the solid diffusion in the battery electrodes is utilized. This method provides an accurate prediction of lithium concentration under the influence of a highly fluctuating current while ensuring computational efficiency. The proposed model is then expressed in an observable state-space form. For an SPM-based linearized reduced order model, the states of the two electrodes and the electrolyte are incorporated in the state-space system with a closed-loop observer design. The issue of weak observability that inherently exists in such a modeling
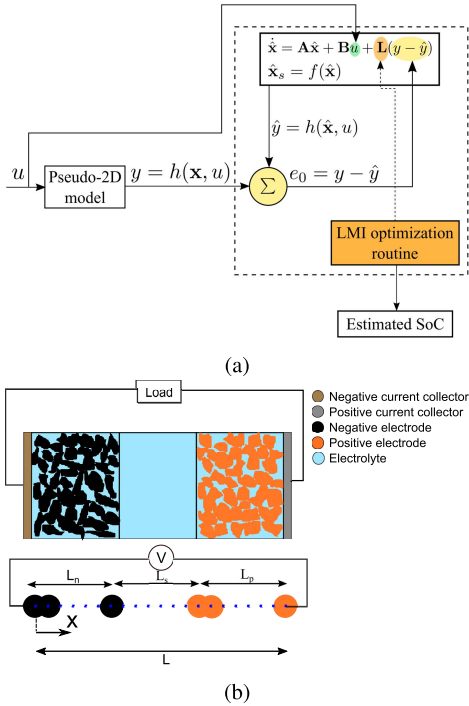
Fig. 1. (a) Block diagram of the proposed SoC estimation algorithm. (b) 1-D schematic representation of the cell.

framework is overcome by computing some of the states as secondary states. Thereby, the approximation involving a linear relationship between the surface concentration of the two electrodes or the usage of an open-loop observer to overcome nonobservability is avoided. In this work, the variation in the model parameters due to changes in temperature, modeling inaccuracies, and the presence of measurement noise is taken into consideration. A robust nonlinear observer is developed to estimate the SoC based on the proposed COSPM. The LMI-based observer design has found a wide variety of applications in control engineering [2], [44], [45] due to their high computational efficiency. The proposed observer's main theoretical contribution is the handling of the nonlinear output function for an uncertain dynamical system, with structural uncertainty and measurement noise, in a linear matrix inequality (LMI) framework. An optimal value of the observer feedback parameter is computed by solving a convex optimization problem with LMI constraints. Thus, the combination of the proposed observer and the improved SPM will provide reliable and a robust estimate of SoC under large parametric variability, measurement noise, and high fluctuations in the current signal.

II. PROPOSED CONTROL-ORIENTED SINGLE-PARTICLE MODEL

This section provides a detailed description of the physics-based modeling of the lithium-ion cell dynamics. It is further divided into two subsections. While the first subsection deals with an improved version of the SPM, the second one presents the state-space formulation of the COSPM. In addition, the definition of SoC is provided in the second subsection. A high-fidelity COSPM-based nonlinear observer is proposed in this

work, as illustrated in Fig. 1(a). Fig. 1(a) depicts the scheme of the observer-based SoC estimation algorithm that takes the current and voltage information as inputs and provides the real-time estimation of the internal states as its output. $\hat{x}$ and $\hat{x}_s$ represent the primary and secondary states of the state-space model, respectively. While the primary states are determined by solving the state-space matrix equation, the secondary states have a linear dependence on these primary states. The output voltage of the high-fidelity P2D model is considered to be representative of the voltage measurement from the real cell.

A. Improved Single-Particle Model

The P2D representation of the cell is provided in Fig. 1(b). The corresponding cell voltage is given as the potential difference between the two current collectors. Considering the geometry in Fig. 1(b), the P2D model writes the cell voltage for the cell as

$$V_{\text{cell}} = \phi_{s,p}(L) - \phi_{s,n}(0) = \eta_p(L) - \eta_n(0) + U_p(L) - U_n(0)$$
$$+ \phi_{e,p}(L) - \phi_{e,n}(0) \quad (1)$$

where overpotential $\eta = \phi_s - \phi_e - U$. Hence, it is clear from (1) that the spatial variation in the overpotential, OCP U, and the ionic potential ϕ_e need to be considered in any reduced-order model so that it is able to predict the cell voltage accurately.

The conventional SPM includes the following assumptions: 1) the electrodes are regarded to be composed of uniform-sized spherical particles; 2) the current density is uniform across the electrode; and 3) the electrolyte offers no limitations to the transport of ions. Though this model can predict cell voltages reasonably for low C-rates, it is inaccurate for C-rates greater than $C/2$ [13]. To overcome this limitation, a few variants that incorporate electrolyte dynamics in SPM have been developed. However, these variants incorporate only the spatial variation in the ionic potential [16], [17], [19].

In a recent work [13], it is demonstrated that the model can be improved by including the spatial variation of overpotential and OCP. Considering these spatial variations, the following modified cell voltage equation is proposed:

$$V_{\text{cell}}(t)$$
$$= \frac{RT}{\alpha_a F} \sinh^{-1} \left[-\frac{I_{\text{app}}(t)}{2a_{s,p} F L_p j_{0,p}(\bar{C}_{s,p}(t))} \right]$$
$$+ U_p(\bar{C}_{s,p}(t)) - \frac{RT}{\alpha_a F} \sinh^{-1} \left[\frac{I_{\text{app}}(t)}{2a_{s,n} F L_n j_{0,n}(\bar{C}_{s,n}(t))} \right]$$
$$- U_n(\bar{C}_{s,n}(t)) - I \left[\frac{L_p}{3\kappa_p^{\text{eff}}} + \frac{L_s}{\kappa_s^{\text{eff}}} + \frac{L_n}{3\kappa_n^{\text{eff}}} + \frac{L_p}{3\sigma_p^{\text{eff}}} + \frac{L_n}{3\sigma_n^{\text{eff}}} \right]$$
$$- \frac{RT(t_+^0 - 1)}{F} \left\{ \frac{2L_n}{3} \left[\frac{1}{C_e} \frac{\partial C_e}{\partial x} \right] \bigg|_{x=L_n^-} + L_s \left[\frac{1}{C_e} \frac{\partial C_e}{\partial x} \right] \bigg|_{x=L_n^+} \right.$$
$$+ L_s \left[\frac{1}{C_e} \frac{\partial C_e}{\partial x} \right] \bigg|_{x=L_n+L_s^-}$$
$$\left. + \frac{2L_p}{3} \left[\frac{1}{C_e} \frac{\partial C_e}{\partial x} \right] \bigg|_{x=L_n+L_s^+} \right\} \quad (2)$$

where the first and third terms on the right-hand side represent the averaged overpotentials, and the second and fourth terms

Phase	Governing equations	Boundary conditions	Initial conditions
Electrolyte	$\epsilon_{e,i} \frac{\partial C_e}{\partial t} = \frac{\partial}{\partial x}\left(D_{e,i}^{\text{eff}} \frac{\partial C_e}{\partial x}\right) + a_{s,i}j_{f,i}\left(1 - t_+^0\right) \quad i \in \{n, p\}$ $\epsilon_{e,s} \frac{\partial C_e}{\partial t} = \frac{\partial}{\partial x}\left(D_{e,s}^{\text{eff}} \frac{\partial C_e}{\partial x}\right)$	$-D_{e,n}^{\text{eff}} \frac{\partial C_e}{\partial x}\Big|_{x=0+} = 0$ $-D_{e,n}^{\text{eff}} \frac{\partial C_e}{\partial x}\Big|_{x=L_n^-} = -D_{e,s}^{\text{eff}} \frac{\partial C_e}{\partial x}\Big|_{x=L_n^+}$ $-D_{e,s}^{\text{eff}} \frac{\partial C_e}{\partial x}\Big|_{x=L_n+L_s^-} = -D_{e,p}^{\text{eff}} \frac{\partial C_e}{\partial x}\Big|_{x=L_n+L_s^+}$ $-D_{e,p}^{\text{eff}} \frac{\partial C_e}{\partial x}\Big|_{x=L^-} = 0$	$C_e = C_{0,e}$
Electrode	$\frac{\partial C_{p,i}}{\partial t} = D_{s,i}\left[\frac{\partial^2 C_{p,i}}{\partial r^2} + \frac{2}{r}\frac{\partial C_{p,i}}{\partial r}\right] \quad i \in \{n, p\}$	$\frac{\partial C_{p,i}}{\partial r}\Big|_{r=0} = 0$ $-D_{s,i} \frac{\partial C_{p,i}}{\partial r}\Big|_{r=R_s} = j_{f,i}$	$C_{p,i} = C_{0,i}$

represent the averaged OCP for the positive and the negative electrodes, respectively. The combined effect of the spatial variation of the ionic potential, overpotential, and OCP results in a difference in the predicted cell voltage from the SPM and is described by the last two terms of the equation. I is the applied current density. As a convention, the discharge current is taken to be positive in this work. The lithium concentration at the surface of the electrode particle $\bar{C}_{s,i}$ is obtained by solving the corresponding diffusion equation under the assumption of a uniform current density. Furthermore, σ_i^{eff} is the electronic conductivities of the solid electrodes, and κ_i^{eff} is the ionic conductivities of the electrolyte in each constituent domain $i \in \{n, s, p\}$. This output voltage equation has been shown to predict the cell voltage within 2% of the P2D model [13] and is henceforward used in the observer design in this work.

The diffusion equation for the electrode particles along with the boundary conditions is provided in Table I. The corresponding semianalytical solution results in the surface lithium concentration, as given by [29]

$$\bar{C}_{s,i} = C_{\text{avg},i} + \sum_{m=1}^{N_i} Q_{m,i} + \epsilon_{N_i} \tag{3}$$

where $C_{\text{avg},i}$ is the average lithium concentration and $\sum_{m=1}^{N_i} Q_{m,i}$ represents the summation of the transient concentration distribution existing within the electrode particles due to different diffusion scales. Furthermore, N_i is the number of terms retained in the truncated infinite series. $C_{\text{avg},i}$ and $Q_{m,i}$ are obtained using the following set of ordinary differential equations [13]:

$$\frac{dC_{\text{avg},i}}{dt} = -\frac{3j_{f,i}}{R_{s,i}} \tag{4}$$

$$\frac{dQ_{m,i}}{dt} = -\frac{2j_{f,i}}{R_{s,i}} - \frac{\lambda_m^2 D_{s,i}}{R_{s,i}^2} Q_{m,i}. \tag{5}$$

Here, λ_m is the mth solution of the equation $\tan \lambda = \lambda$. The molar flux density $j_{f,i}(t)$ is given by

$$j_{f,i} = \frac{I_i}{a_{s,i}FL_i} \tag{6}$$

where $I_n = I$ and $I_p = -I$. The approximation error in (3) is [29]

$$\epsilon_{N_i} = -\frac{2j_{f,i}R_{s,i}}{D_{s,i}}\left[\left(\frac{1}{10} - \sum_{m=1}^{N_i}\frac{1}{\lambda_m^2}\right)\left[1 - e^{-\lambda_{N_i+1}^2 D_{s,i}t/R_{s,i}^2}\right]\right.$$
$$\left. + \sqrt{\frac{D_{s,i}t}{\pi R_{s,i}^2}}\text{erfc}\left(\lambda_{N_i+1}\sqrt{\frac{D_{s,i}t}{R_{s,i}^2}}\right)\right]. \tag{7}$$

The solution of (5) for a given constant current profile results in an exponentially decaying function with a time constant of $\tau_i(m) = R_{s,i}^2/(D_{s,i}\lambda_m^2)$. Furthermore, the steady-state magnitude of Q_m for a given current is proportional to $\tau_i(m)$. Hence, as the value of λ_m increases (with an increase in the number of terms), the contribution of the state $Q_{m,i}$ in (3) rapidly decreases. A criterion $\tau_i(m = N_i) < 10$ s was proposed to truncate the series in (3) while ensuring good accuracy for highly fluctuating currents [13]. Using this criterion, we can obtain a constraint on λ_m and, thereby, determine the number of terms to be retained. Here, nine and three terms have been used for the negative (graphite) and positive (manganese oxide) electrodes, respectively. The significantly higher diffusion time scale for the negative electrode than that of the positive electrode is the reason for the corresponding requirement of a greater number of terms in the former. The parameters used for the two electrodes are provided in Table II.

The error term in (7) can be further simplified without any significant loss of accuracy. The second term (complementary error term) in (7) is significant only for a very small time interval at the start of cycling and quickly becomes negligible. Similarly, the exponential component in the first term on the right-hand side of (7) also quickly approaches zero as it is a decaying function in time with a time constant of $\tau_i(m) = R_{s,i}^2/(D_{s,i}\lambda_{N_i+1}^2)$. In our case, the time constants were obtained by $R_{s,i}^2/(D_{s,i}\lambda_{N_i+1}^2) \approx 3$ s for both electrodes. Hence, ignoring the contribution of these terms, we write the simplified error term as

$$\epsilon_{N,i} = -\frac{2j_{f,i}R_{s,i}}{D_{s,i}}\left[\frac{1}{10} - \sum_{m=1}^{N_i}\frac{1}{\lambda_m^2}\right]. \tag{8}$$

The use of (8) simplifies the computation by removing the time-dependent component of the error function and the complementary error function term that requires evaluation of an integral.

In Fig. 2, a comparison of various linear relations used in the literature for the second electrode (here, positive electrode) [10], [11] is made with the proposed model. The FVM-based solution for 100 divisions is considered to be the benchmark as it represents the converged solution of the diffusion equation. We observe that the proposed model considering the diffusion states of both electrodes predicts the lithium-ion concentration in the positive electrode with better accuracy. This improvement can be attributed to the fact that the diffusion time scales for the

TABLE II

MODEL PARAMETERS

| Parameter	Symbol (units)	Negative electrode	Separator	Positive electrode
Maximum solid lithium concentration	$C_{\max,i}$ (mol/m^3)	26390 [46]		22860 [46]
Initial solid lithium concentration	$C_{0,i}$ (mol/m^3)	14820.6		3963.9
Thickness	$L_i (\mu m)$	128 [46]	76 [46]	190 [46]
Electrode diffusion coefficient	$D_{s,i}$ (m^2/s)	3.9×10^{-14} [6]		1×10^{-13} [6]
Electrode particle radius	$R_{s,i}$ (μm)	12.5 [46]		8.5 [46]
Reaction rate constant	k_i	2×10^{-11}		2×10^{-11}
Initial electrolyte lithium concentration	$C_{0,e}$ (mol/m^3)		2000 [46]	
Transference number	t_+^0		0.363 [6]	
Electrolyte diffusion coefficient	D_e (m^2/s)		7.5×10^{-11} [46]	
Ionic conductivity of electrolyte	κ_l (S/m)		0.11 [47]	
Activation energies	$E_{a,D_{s,i}}$ (J/mol)	4×10^3 [46]		2×10^4 [46]
	E_{a,D_e} (J/mol)		1×10^4 [46]	
	E_{a,κ_l} (J/mol)		2×10^4 [46]	
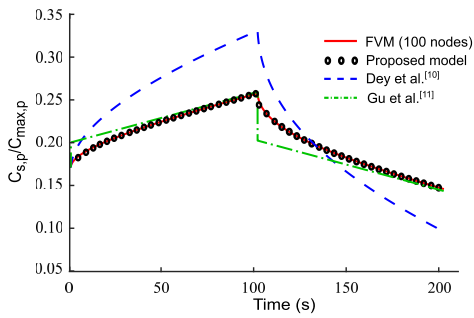
Fig. 2. Comparison of the surface concentration in the second electrode (here, positive) based on proposed state-space system with the linear models used by Dey *et al.* [10] and Gu *et al.* [11].

two electrodes are very different, and hence, using a linear relation between the two surface concentrations is a poor approximation.

The volume-averaged, 1-D diffusion equation for lithium ions for the three cell domains along with the boundary conditions is provided in Table I. In the improved SPM [13], a second-degree polynomial is used to approximate the spatial variation of the electrolyte concentration in the cell components $i \in \{n, s, p\}$

$$\bar{C}_{e,i} = a_{i,0}(t) + a_{i,1}(t)\bar{x}_i + a_{i,2}(t)\bar{x}_i^2 \qquad (9)$$

where

$$\bar{C}_{e,i} = \frac{C_{e,i}}{C_{0,e}}, \quad \bar{x}_n = \frac{x}{L_n}$$

$$\bar{x}_s = \frac{x - L_n}{L_s}, \quad \bar{x}_p = \frac{x - L_n - L_s}{L_p}$$

are nondimensionalized concentration and normalized coordinates. The nine unknown coefficients are obtained by solving the six flux and continuity boundary conditions of the P2D model, along with three integrated conservation equations [13]. This results in a system of differential-algebraic equations given by

$$a_{n,1} = 0 \qquad (10)$$

$$2a_{p,2} + a_{p,1} = 0 \qquad (11)$$

$$\left(\frac{\epsilon_{e,n}}{\epsilon_{e,s}}\right)^{\text{brug}} \frac{L_s}{L_n} \left(2a_{n,2} + a_{n,1}\right) - a_{s,1} = 0 \qquad (12)$$

$$\left(\frac{\epsilon_{e,s}}{\epsilon_{e,p}}\right)^{\text{brug}} \frac{L_p}{L_s} \left(2a_{s,2} + a_{s,1}\right) - a_{p,1} = 0 \qquad (13)$$

$$a_{n,0} + a_{n,1} + a_{n,2} - a_{s,0} = 0 \qquad (14)$$

$$a_{s,0} + a_{s,1} + a_{s,2} - a_{p,0} = 0 \qquad (15)$$

$$\frac{da_{n,0}}{dt} + \frac{1}{2}\frac{da_{n,1}}{dt} + \frac{1}{3}\frac{da_{n,2}}{dt} = \frac{2D_{e,n}^{\text{eff}}}{\epsilon_{e,n}L_n^2}a_{n,2}$$
$$- \frac{I(1-t_+)}{L_n F C_{0,e}\epsilon_{e,n}} \qquad (16)$$

$$\frac{da_{s,0}}{dt} + \frac{1}{2}\frac{da_{s,1}}{dt} + \frac{1}{3}\frac{da_{s,2}}{dt} = \frac{2D_{e,s}^{\text{eff}}}{\epsilon_{e,s}L_s^2}a_{s,2} \qquad (17)$$

$$\frac{da_{p,0}}{dt} + \frac{1}{2}\frac{da_{p,1}}{dt} + \frac{1}{3}\frac{da_{p,2}}{dt} = -\frac{2D_{e,p}^{\text{eff}}}{\epsilon_{e,p}L_p^2}a_{p,2}$$
$$+ \frac{I(1-t_+)}{L_p F C_{0,e}\epsilon_{e,p}}. \qquad (18)$$

B. State-Space Formulation

The state-space formulation for the proposed SPM comprises the states of the negative and positive electrodes and the electrolyte. Incorporating all the twenty-three variables (ten for negative electrode, four for positive electrode, and nine for electrolyte) in the state vector leads to nonobservability. This issue has been overcome in previous works [10], [11] by incorporating the states of a single electrode in the state vector, which is then used to compute the surface concentration of the second electrode based on a linear conservation relationship. However, relating the surface concentrations using a linear relation may not be able to capture the effect of significantly different diffusion time scales that exist for the positive and negative electrodes of a lithium-ion cell. Consequently, such models could be extremely inaccurate for the electrode for which this relation is used to determine the surface concentration. However, this relation is valid in terms of the volume-averaged lithium concentrations of the two electrodes. In addition, the diffusion equations for the electrodes need to be solved separately in order to obtain their surface concentra-

tions. The proposed model considers the individual diffusion equations, thereby improving accuracy. In our proposed model, the average concentration of the positive electrode $C_{\text{avg},p}$ is not incorporated in the state vector and is instead computed by considering species conservation of lithium (i.e., total lithium in the electrodes is conserved)

$$\epsilon_{s,n} L_n C_{\text{avg},n} + \epsilon_{s,p} L_p C_{\text{avg},p}$$
$$= \epsilon_{s,n} L_n C_{0,n} + \epsilon_{s,p} L_p C_{0,p}. \quad (19)$$

This resolves the issue of nonobservability of the state-space model of the lithium-ion cell. The diffusion states $Q_{m,i}$ for the positive electrode along with all states for the negative electrode are retained in the state vector (primary states), and their solution is used to compute the surface concentration for the positive electrode (secondary state) using the following relation:

$$\bar{C}_{s,p} = \frac{\epsilon_{s,n} L_n}{\epsilon_{s,p} L_p} C_{0,n} + C_{0,p} - \frac{\epsilon_{s,n} L_n}{\epsilon_{s,p} L_p} C_{\text{avg},n} + \sum_{m=1}^{3} Q_{m,p}. \quad (20)$$

The above equation has been obtained by substituting the expression for $C_{\text{avg},p}$ from (19) in (3).

Similar to the issue in the solid phase, the inclusion of all the states related to the electrolyte also renders the system as nonobservable. The terms leading to this nonobservability were identified to be $a_{n,0}$, $a_{s,0}$, and $a_{p,0}$. One may choose any six of the nine electrolyte states as secondary variables and compute them algebraically from (10) to (15). However, the three ordinary differential equations in (16)–(18) force retention of three primary states with at least one being an $a_{i,0}$, as only two of the three $a_{i,0}$ states can be replaced using (14) and (15). Hence, the conservation of lithium ions in the electrolyte is used to obtain an additional equation. The state $a_{n,0}$ is computed as a secondary variable using

$$\epsilon_{e,n} L_n C_{\text{avg},e,n} + \epsilon_{e,s} L_s C_{\text{avg},e,s} + \epsilon_{e,p} L_p C_{\text{avg},e,p}$$
$$= (\epsilon_{e,n} L_n + \epsilon_{e,s} L_s + \epsilon_{e,p} L_p) C_{0,e}. \quad (21)$$

Obtaining the average concentration of lithium ions in constituent domains by integrating (9) and substituting in the previous equation, we get

$$\epsilon_{e,n} L_n \left(a_{n,0} + \frac{a_{n,1}}{2} + \frac{a_{n,2}}{3} \right) + \epsilon_{e,s} L_s \left(a_{s,0} + \frac{a_{s,1}}{2} + \frac{a_{s,2}}{3} \right)$$
$$+ \epsilon_{e,p} L_p \left(a_{p,0} + \frac{a_{p,1}}{2} + \frac{a_{p,2}}{3} \right) = \epsilon_{e,n} L_n + \epsilon_{e,s} L_s + \epsilon_{e,p} L_p. \quad (22)$$

Equations (10)–(16) can be used to reformulate (thereby, removing nonobservability arising due to $a_{s,0}$ and $a_{p,0}$). Equations (17) and (18) give

$$-\left[\frac{2}{3} + \left(\frac{\epsilon_{e,n}}{\epsilon_{e,s}} \right)^{\text{brug}} \frac{L_s}{L_n} \right] \frac{da_{n,2}}{dt} - \left[\frac{1}{3} + \left(\frac{\epsilon_{e,p}}{\epsilon_{e,s}} \right)^{\text{brug}} \frac{L_s}{2L_p} \right] \frac{da_{p,1}}{dt}$$
$$= \frac{2D_{e,n}}{\epsilon_{e,n} L_n^2} a_{n,2} + \frac{D_{e,p}}{\epsilon_{e,p} L_p^2} a_{p,1} + \frac{(1 - t_+^0)}{FC_{0,e}}$$
$$\times \left[\frac{1}{L_n \epsilon_{e,n}} + \frac{1}{L_p \epsilon_{e,p}} \right] I, \quad (23)$$

$$-\left[\frac{2}{3} + \left(\frac{\epsilon_{e,n}}{\epsilon_{e,s}} \right)^{\text{brug}} \frac{2L_s}{3L_n} \right] \frac{da_{n,2}}{dt} - \left(\frac{\epsilon_{e,p}}{\epsilon_{e,s}} \right)^{\text{brug}} \frac{L_s}{6L_p} \frac{da_{p,1}}{dt}$$
$$= \left[\frac{2D_{e,n}}{\epsilon_{e,n} L_n^2} + \frac{2D_{e,s}}{\epsilon_{e,s} L_s^2} \left(\frac{\epsilon_{e,n}}{\epsilon_{e,s}} \right)^{\text{brug}} \frac{L_s}{L_n} \right] a_{n,2} - \frac{D_{e,s}}{\epsilon_{e,s} L_s^2}$$
$$\times \left(\frac{\epsilon_{e,p}}{\epsilon_{e,s}} \right)^{\text{brug}} \frac{L_s}{L_p} a_{p,1} + \frac{(1 - t_+^0)}{FC_{0,e}} \frac{1}{L_n \epsilon_{e,n}} I. \quad (24)$$

For the electrolyte, the states $a_{n,2}$ and $a_{p,1}$ are incorporated in the state vector using (23) and (24). The remaining states are computed as secondary states using the algebraic (10)–(15) and (22). Using (4), (5), (23), and (24), the state-space system can be written as

$$\dot{\mathbf{x}} = \mathbf{A}\mathbf{x} + \mathbf{B}u \quad (25)$$

where $\mathbf{x} = \left[\mathbf{x}_n, \mathbf{x}_p, \mathbf{x}_e \right]^T \in \mathbb{R}^{15 \times 1}$, $\mathbf{B} = \left[\mathbf{B}_n, \mathbf{B}_p, \mathbf{M}_e^{-1} \mathbf{B}_e \right]^T \in \mathbb{R}^{15 \times 1}$, $u = I$, and

$$\mathbf{A} = \text{diag}\left(\mathbf{A}_n, \mathbf{A}_p, \mathbf{M}_e^{-1} \mathbf{A}_e \right) \quad (26)$$

where $diag(e_1, e_2, \ldots)$ denotes diagonal matrix with diagonal entries $e_1, e_2, \ldots$ Here, $\mathbf{x}_n = [C_{\text{avg},n}, Q_{1,n}, Q_{2,n}, \ldots, Q_{9,n}]^T$, $\mathbf{x}_p = [Q_{1,p}, Q_{2,p}, Q_{3,p}]^T$, and $\mathbf{x}_e = [a_{n,2}, a_{p,1}]^T$. $\mathbf{O}$ is a null matrix. In addition, the output equation is given by (2), where

$$C_e(0) = C_{0,e} a_{n,0} \quad (27)$$
$$C_e(L) = C_{0,e} (a_{p,0} + a_{p,1} + a_{p,2}). \quad (28)$$

In our proposed formulation, any additive uncertainty in the system matrix $\mathbf{A}$ and the input matrix $\mathbf{B}$ in (25) can be accounted for by rewriting the state-space model in the following form:

$$\mathbf{\dot{x}}(t) = (\mathbf{A} + \Delta\mathbf{A}(t))\mathbf{x}(t) + (\mathbf{B} + \Delta\mathbf{B}(t))u(t) \quad (29)$$

with a scalar nonlinear output map in (2) rewritten as

$$y(t) = h(\mathbf{x}(t), u(t)) + \xi_y \quad (30)$$

where state $\mathbf{x} \in \mathbb{R}^n$, input $u \in \mathbb{R}$, $\mathbf{A} \in \mathbb{R}^{n \times n}$ is the nominal system matrix, $\mathbf{B} \in \mathbb{R}^{n \times 1}$ is the input vector, $\Delta\mathbf{A} \in \mathbb{R}^{n \times n}$ denotes the uncertainty in the system matrix, $\Delta\mathbf{B} \in \mathbb{R}^n$ represents the uncertainty in the input matrix, and $h(\mathbf{x}, u) \in \mathbb{R}$ is the output function. The details about system matrix $\mathbf{A}$, input matrix $\mathbf{B}$, and the output $h(\mathbf{x}, u)$ are provided in Appendix B. In (30), ξ_y denotes the uncertainty in the measurement of the output. The output function (30) can be rewritten in the following form as:

$$y = \mathbf{K}_{\min}\mathbf{x} + \bar{h}(\mathbf{x}, u) + \xi_y \quad (31)$$

where $\bar{h}(\mathbf{x}, u) = h(\mathbf{x}, u) - \mathbf{K}_{\min}\mathbf{x}$.

The SoC for the proposed physics-based reduced-order model can be defined as

$$\text{SoC} = \frac{C_{\text{avg},n} - C_{n,\text{SoC}=0}}{C_{n,\text{SoC}=1} - C_{n,\text{SoC}=0}}. \quad (32)$$

The SoC of the lithium-ion cell is defined to be 0 and 1 at 3 and 4.2 V, respectively. $C_{n,\text{SoC}=0}$ and $C_{n,\text{SoC}=1}$ are the concentrations of lithium ions in the negative electrode at these SoC levels. Furthermore, the nominal cell capacity (Q) is defined as the charge capacity obtained on discharging the lithium-ion cell from 4.2 to 3 V at the $C/30$ rate at 25 °C.

III. Design of the Robust Nonlinear Observer

In this section, a robust nonlinear observer is proposed for the SoC estimation problem using the COSPM in the LMI framework. The observer design in [2] was based on ECM that involved a transformation of the nonlinear output map into a linear one with the assumption that the change in the input current is negligible. This assumption is restrictive for dynamic driving cycles involving huge fluctuations in the current profile. To resolve this issue, an optimal feedback parameter of the observer is obtained by solving an LMI optimization problem. The observer ensures fast convergence of the estimated SoC to its true value in the presence of bounded parametric uncertainty. Furthermore, the proposed observer design has a lower computational cost than its stochastic filter counterparts [2]. Consider an extended Luenberger-like observer [48] as

$$\dot{\hat{\mathbf{x}}}(t) = \mathbf{A}\hat{\mathbf{x}} + \mathbf{B}u + \mathbf{L}\big[y - \mathbf{K}_{\min}\hat{\mathbf{x}} - \bar{h}(\hat{\mathbf{x}}, u)\big] \qquad (33)$$

where $\mathbf{L}$ is the observer gain matrix and $\bar{h}(\hat{\mathbf{x}}, u) = h(\hat{\mathbf{x}}, u) - \mathbf{K}_{\min}\hat{\mathbf{x}}$. The error in the state estimation is defined as

$$\mathbf{e}_o := \mathbf{x} - \hat{\mathbf{x}}. \qquad (34)$$

Differentiating the estimation error in (34), and using (29) and (33) yield

$$\dot{\mathbf{e}}_o = \dot{\mathbf{x}} - \dot{\hat{\mathbf{x}}} = [\mathbf{A} - \mathbf{LK}_{\min}]\mathbf{e}_o - \mathbf{L}\phi(\mathbf{x}, \hat{\mathbf{x}}, u) + \Delta\mathbf{A}\mathbf{x} + \Delta\mathbf{B}u \qquad (35)$$

where $\phi(\mathbf{x}, \hat{\mathbf{x}}, u) = \bar{h}(\mathbf{x}, u) - \bar{h}(\hat{\mathbf{x}}, u)$. The following assumptions are considered for the observer design.

1) The Jacobian of the nonlinear output map $h(\mathbf{x}, u)$ is bounded as

$$\mathbf{K}_{\min} \leq \frac{\partial h(\mathbf{x}, u)}{\partial \mathbf{x}} \leq \mathbf{K}_{\max} \qquad (36)$$

where $\mathbf{K}_{\min}$ and $\mathbf{K}_{\max}$ are elementwise lower and upper bounds of the Jacobian, known *a priori*.

2) The nonlinear function $h(\mathbf{x}, u)$ satisfies the Lipschitz condition [44]

$$\|h(\mathbf{x}, u) - h(\hat{\mathbf{x}}, u)\| \leq L_h\|\mathbf{x} - \hat{\mathbf{x}}\| \qquad (37)$$

where '$\|.\|$' denotes the euclidean norm and $L_h > 0 \in \mathbb{R}$ is the Lipschitz constant. The expressions for $h(\mathbf{x}, u)$ and $h(\hat{\mathbf{x}}, u)$ can be obtained from (31) and (33), respectively, and substituted for $\phi(\mathbf{x}, \hat{\mathbf{x}}, u)$. Using the Lipschitz condition in (37), $\phi(\mathbf{x}, \hat{\mathbf{x}}, u)$ can be bounded as

$$\|\phi(\mathbf{x}, \hat{\mathbf{x}}, u)\| \leq (L_h + \|\mathbf{K}_{\min}\|) \|\mathbf{e}_o\|. \qquad (38)$$

3) The matrices $\Delta\mathbf{A}$ and $\Delta\mathbf{B}$ are bounded

$$\|\Delta\mathbf{A}\| \leq \delta_a, \|\Delta\mathbf{B}\| \leq \delta_b \text{ where } \delta_a > 0 \in \mathbb{R}, \quad \delta_b > 0 \in \mathbb{R}. \qquad (39)$$

4) The state $\mathbf{x}$, the input u, and the output uncertainty ξ_y satisfy the following bounds:

$$\|\mathbf{x}\| \leq X_+, \|u\| \leq U_+ \|\xi_{\mathbf{y}}\| \leq \mathcal{Y}_+$$
$$\text{where } X_+ > 0 \in \mathbb{R}, \quad U_+ > 0 \in \mathbb{R}, \quad \mathcal{Y}_+ > 0 \in \mathbb{R}. \qquad (40)$$

5) The pair $(\mathbf{A},\mathbf{C})$ of the system in (29) is observable where the matrix $\mathbf{C}$ represents the linearization of the nonlinear output function $y = h(\mathbf{x}, u)$ in (30) at a particular operating point.

The Jacobian of the nonlinear output function $h(\mathbf{x}, u)$ in (30) is computed numerically using MATLAB. The minimum and the maximum of the Jacobian, $\mathbf{K}_{\min}$ and $\mathbf{K}_{\max}$ in Assumption 1, are computed using the bounds of the underlying parameters and variables. These bounds are determined through various dynamic tests, such as FTP75 and US06 tests. Since the output function $h(\mathbf{x}, u)$ is continuous, differentiable, and monotonic, and its Jacobian is bounded, it satisfies the Lipschitz condition in Assumption 2. The details about the computation of ΔA and ΔB are provided in Remark 3. The terminal voltage of a lithium-ion cell can never be unbounded for a bounded input current. Thus, Assumption 4 is a bounded-input–bounded-output (BIBO) criterion for the system [see (25)], which states that the states, input, and measurement noise are bounded [2]. The numerical variables of the bounds of the states, the input, and the measurement noise are determined through various tests.

The convergence and stability analysis of the estimation error dynamics in (35) are provided in the following theorem. The computation of the observer gain $\mathbf{L}$ is obtained by solving a convex optimization problem with LMI constraints.

Theorem 1: Consider the uncertain dynamical system in (29) with a nonlinear output map (31), which admits an observer (33), where the above stated Assumptions 1–5 hold true. If there exists a symmetric positive definite matrix $\mathbf{P} = \mathbf{P}^T > 0$, an observer gain matrix $\mathbf{L}$, and positive constants $\alpha > 0, \varepsilon_i > 0, i = 1, 2$, such that the following matrix inequality is satisfied:

$$\mathbf{W}_3(\mathbf{P}, \mathbf{L}|\alpha, \varepsilon_1, \varepsilon_2)$$
$$= \begin{bmatrix} \Lambda_3 & -\mathbf{PL} & \mathbf{P} & -\mathbf{PL} \\ * & -\varepsilon_1\mathbf{I}_{n\times n} & \mathbf{0} & \mathbf{0} \\ * & * & -\varepsilon_2\mathbf{I}_{n\times n} & \mathbf{0} \\ * & * & * & -\varepsilon_3\mathbf{I}_{n\times n} \end{bmatrix} < \mathbf{0} \qquad (41)$$

then the state estimation error $\mathbf{e}_o(t)$ exponentially converges to a convex set, where $\Lambda_3 = (\mathbf{A} - \mathbf{LK}_{\min})^T\mathbf{P} + \mathbf{P}(\mathbf{A} - \mathbf{LK}_{\min}) + \alpha\mathbf{P} + \varepsilon_1(L_h + \mathbf{K}_{\min})\mathbf{I}_{n\times n}$ and "$*$" represents the symmetric elements of the matrix, "$[.]^T$" is the transpose operator, and "$|$" denotes given.

The stability analysis and the proof of the Theorem 1 are provided in Appendix A for reference. It is important to note that the inequality in (41) is a bilinear matrix inequality (BMI) due to the presence of some nonlinear terms $\mathbf{PLK}_{\min}$ and $\mathbf{K}_{\min}^T\mathbf{L}^T\mathbf{P}^T$, where $\mathbf{P}$ and $\mathbf{L}$ are unknown variables. The BMI is then transformed to LMI by the following corollary.

Corollary 1: Introducing the change of variable $\mathbf{Y} := \mathbf{PL}$ in (41), one can convert the BMI into LMI inequality as follows:

$$\tilde{\mathbf{W}}_3(\mathbf{P}, \mathbf{Y} \mid \alpha, \varepsilon_1, \varepsilon_2, \varepsilon_3)$$
$$= \begin{bmatrix} \tilde{\Lambda}_3 & -\mathbf{Y} & \mathbf{P} & -\mathbf{Y} \\ * & -\varepsilon_1\mathbf{I}_{n\times n} & \mathbf{0} & \mathbf{0} \\ * & * & -\varepsilon_2\mathbf{I}_{n\times n} & \mathbf{0} \\ * & * & * & -\varepsilon_3\mathbf{I}_{n\times n} \end{bmatrix} < \mathbf{0} \qquad (42)$$

and $\tilde{\Lambda}_3 = \mathbf{P}(\mathbf{A} + (\alpha/2)\mathbf{I}_{n\times n}) + (\mathbf{A} + (\alpha/2)\mathbf{I}_{n\times n})^T\mathbf{P} - \mathbf{YK}_{\min} - \mathbf{K}_{\min}^T\mathbf{Y}^T + \varepsilon_1(L_h + \|\mathbf{K}_{\min}\|)^2\mathbf{I}_{n\times n}$.

The nonlinear terms $\mathbf{PLK}_{\min}$ and $\mathbf{K}_{\min}^T \mathbf{L}^T \mathbf{P}$ in (41) have been converted to linear terms $\mathbf{YK}_{\min}$ and $\mathbf{K}_{\min}^T \mathbf{Y}^T$ in (42), respectively. It is worth mentioning at this stage that the state estimation error $\mathbf{e}_o(t)$ is bounded in the set for all time. Another corollary is provided to compute the optimal value for the observer gain matrix $\mathbf{L}^*$ by minimizing the volume of the convex set within which the state estimation error is guaranteed to be confined by Theorem 1.

Corollary 2: The optimal observer feedback parameter $\mathbf{L}^*$ can be numerically calculated if the following LMI optimization problem is solved:

$$\underset{\mathbf{P}>0,\mathbf{L},\alpha>0,\varepsilon_1>0,\varepsilon_2>0}{\text{minimize}} \quad \text{tr}(\mathbf{P}_{\text{attr}}) \tag{43}$$

while satisfying the following inequality:

$$\mathbf{P} > 0, \quad \tilde{\mathbf{W}}_3(\mathbf{P}, \mathbf{Y}|\alpha, \varepsilon_1, \varepsilon_2, \varepsilon_3) < \mathbf{0} \tag{44}$$

where the operator $\text{tr}(.)$ represents the trace of a matrix, $\mathbf{P}_{\text{attr}} = \alpha \mathbf{P}/c$, and $c = \varepsilon_2(\delta_a^2 X_+^2 + \delta_b^2 U_+^2) + \varepsilon_3 \mathcal{Y}_+^2$.

IV. RESULTS

Simulations were carried out to evaluate the efficacy of the proposed observer (33) for estimating SoC under different current and temperature conditions. As shown in Fig. 1(a), the observer utilizes the current and voltage information to provide the real-time estimation of the primary states. The secondary states are determined from the primary states. The estimation results are also compared with the SoC predictions of the P2D model that is solved using COMSOL Multiphysics. The temperature dependence of the transport parameters has been assumed to follow Arrhenius relationships with their activation energies given in Table II. The numerical values of the parameters for the COSPM appearing in the matrices $\mathbf{A}$ and $\mathbf{B}$ in (29) and the observer equation in (33) are given in Table II. The negative and positive electrodes are considered to be graphite and manganese-oxide ($Li_yMn_2O_4$), respectively. The electrolyte is 1-M $LiPF_6$ in 2:1 EC:DMC. The numerical values for the optimal feedback parameter $\mathbf{L}^* = [l_i]^T, l_1 = 376, l_i = -27.63, i = 2, \ldots, 14$, in (43) for the proposed observer are computed by solving the convex optimization problem presented in (43). The values of the design parameters are chosen to be $\alpha = 5 \times 10^4, \varepsilon_1 = 1 \times 10^{13}, \varepsilon_2 = 1 \times 10^{-17}, \varepsilon_3 = 1 \times 10^{-10}, L_h = 0.01$, and $\mathbf{K}_{\min} = [k_i], k_i = 0.0001, i = 1, \ldots, 6$. While the parameters $L_h, \mathbf{K}_{\min}, \delta_a = 0.2884$, and $\delta_b = 0.5383$ are computed using the uncertainty bounds of the system dynamics, the numerical values of the design parameters $\alpha, \varepsilon_i, i = 1, \ldots, 3$, are chosen such that the solution to the LMI problem (43) is feasible. The OCP–SoC relationship for the anode and the cathode are taken from [47] as

$$U_n(x_n) = -0.16 + 1.32 \exp(-3x_n) + 10 \exp(-2000x_n) \tag{45}$$

$$\begin{aligned} U_p(x_p) &= 4.19829 + 0.565661 \tanh(-14.5546 \, x_p + 8.60942) \\ &\quad - 0.0275479 \left[\frac{1}{(0.998432 - x_p)^{0.492465}} - 1.90111 \right] \\ &\quad - 0.157123 \exp(-0.04738 \, x_p^8) \\ &\quad + 0.810239 \exp\left[-40(x_p - 0.133875)\right] \end{aligned} \tag{46}$$

where $x_n = C_{s,n}/C_{\max,n}$ and $x_p = C_{s,p}/C_{\max,p}$.
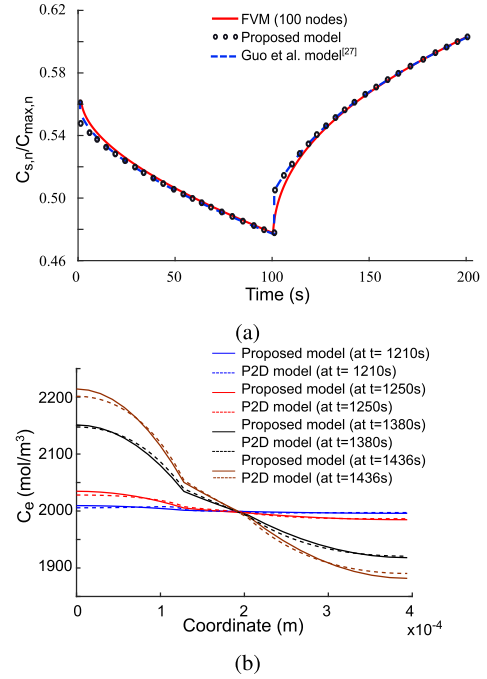

Fig. 3. Verification of the proposed model. Comparison of (a) surface lithium concentration for the negative electrode based on the proposed semianalytical model with FVM and Guo and White's [29] model for a 3C-pulse test and (b) lithium concentration in the electrolyte for the polynomial model with the P2D model for the US06 drive cycle.

A. Verification of the Proposed Model

A comparison of the lithium surface concentration for the proposed semianalytical diffusion model to that of FVM with 100 nodes demonstrates the applicability of the error simplification. The simulation consists of the application of a 3-C rate discharge current for 100 s followed by a 3-C rate charge current for 100 s. As shown in Fig. 3(a) for the negative electrode, the proposed model is in excellent agreement with FVM and results of [29]. The maximum absolute difference between the SoCs of the proposed model and [29] is bounded within 0.01. Furthermore, the two models provide identical surface concentration predictions after the first 25 s, thereby validating the fast convergence of the error term in (8) to that of (7).

The electrolyte concentration distribution across the cell domain obtained from the polynomial model is verified against that of the P2D model for the US06 drive cycle. The discharge current profile consists of a rest period of 20 minutes, followed by the US06 drive test. The maximum current reached in the US06 test was 3 C. Fig. 3(b) demonstrates that the polynomial approximation is in excellent agreement with the P2D model. Though being a highly simplified representation, the former closely captures the diffusion dynamics of the electrolyte.

B. Evaluation of Nominal Performance of the Observer

Two dynamic tests, FTP75 and US06, are considered to evaluate the effectiveness of the robust observer in estimating the SoC at 15 °C, 25 °C, 35 °C, and 45 °C. These are standard drive cycles used for testing of light-duty vehicles [2]. The FTP75 test profile represents the transient driving behavior
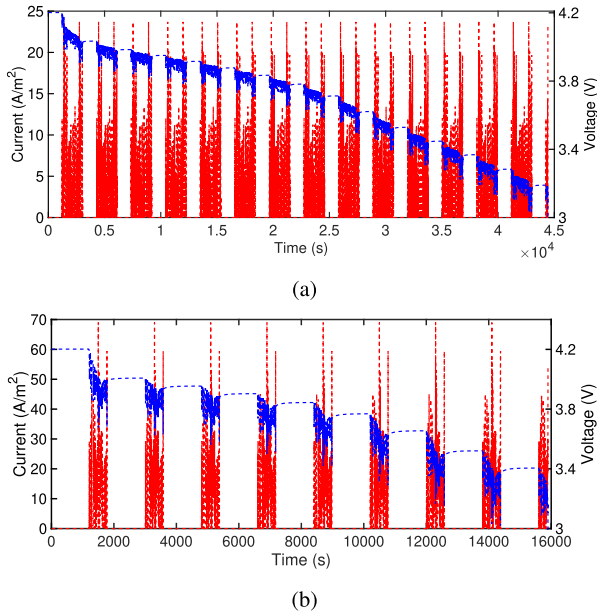
Fig. 4. Input current and corresponding output voltage for (a) FTP75 and (b) US06 tests at 25 °C.

TABLE III
PERFORMANCE INDICES (PIs), ME AND INTEGRAL SQUARE ERROR (ISE), FOR THE SoC ESTIMATION BY THE PROPOSED OBSERVER FOR FTP75 AND US06 DYNAMIC TESTS AT 15 °C, 25 °C, 35 °C, AND 45 °C AT 3-, 5-, AND 7-C CURRENT RATES

Tests	Temperature (°C)	ISE at different C-Rate		
		3C	5C	7C
FTP75	−10°C	3.917	4.864	5.639
	0°C	2.788	3.276	3.637
	15°C	1.812	1.985	1.922
	25°C	1.812	1.938	1.912
	35°C	1.764	1.856	1.846
	45°C	1.714	1.784	1.854
US06	−10°C	6.529	7.108	6.623
	0°C	4.059	4.434	4.024
	15°C	1.895	2.455	2.158
	25°C	1.899	2.337	2.085
	35°C	1.862	2.187	2.467
	45°C	1.939	2.170	2.442

with a large number of start-stops experienced while driving in cities. The US06 test profile comprises rapid acceleration and high-speed driving characteristics, and is a representation of the driving behavior on highways. However, the dynamic tests are also conducted at −10 °C and 0 °C to investigate the observer's performance at low temperatures. The input current and voltage data of the P2D model were obtained for the FTP75 and US06 after ensuring that the initial SoC was 100%. The input current and output voltage curves for the two tests are provided in Fig. 4 for 25 °C. The details of the estimation results for the dynamic tests are given in the following.

Remark 1: For all the simulations, it is assumed that the high-fidelity P2D model of the lithium-ion cell represents the physical system. The P2D model is the most successful electrochemical model for lithium-ion cells and has been thoroughly tested and validated [7], [47], [49]. It has also found application as the representation for the real cell in estimation-based works [50], [51]. As a standard practice in the literature [2], [3], the coulomb counting method (CCM) is assumed to provide the "true" SoC for the P2D model. The CCM is known to give precise SoC values since the initial SoC is known *a priori* exactly in a controlled environment.

1) FTP75 Test: Fig. 5(a) illustrates a comparison of the temporal variation of the estimated SoC obtained from the proposed observer with the true SoC (P2D model) at −10 °C, 0 °C, 15°C, 25 °C, 35 °C, and 45 °C for FTP75 tests with maximum current of 3-C rate. The initial guess for the SoC is considered to be 0.6. From Fig. 5(a), it is evident that, despite an initial error of 40% in the initial SoC estimate, the observer could faithfully track the true SoC using the voltage measurements from the P2D model within 50 s at different temperatures. The ISE of SoC estimation error for each case is reported in Table III. The SoC estimation errors

provided by the COSPM-based observer remain bounded within a maximum error bound of 0.01 for 15 °C, 25 °C, 35 °C, and 45 °C. However, the maximum SoC errors are within 0.025 at extremely low temperatures of −10 °C and 0°C. During the FTP75 tests, the terminal voltage profiles at different temperatures are shown in Fig. 5(b). A maximum variation of 20 mV in the terminal voltage profiles is recorded against the variation of the order 10^{-4} in the estimated SoC signals at different temperatures.

Remark 2: The P2D model was implemented in COMSOL at various temperatures with temperature-dependent OCP transport properties. The corresponding output cell voltage is utilized in the estimation algorithm as the real-time measurement data.

2) US06 Test: The US06 dynamic test is considered to evaluate the observer's performance for a driving cycle with high fluctuations in the input current profile with a maximum current of the 3-C rate. The time evolution of the estimated SoC at −10 °C, 0 °C, 15 °C, 25 °C, 35 °C, and 45 °C utilizing the terminal voltage measurements of the P2D model is depicted in Fig. 5(c). The initial states of the proposed observer are kept the same as in the previous case. From Fig. 5(c), it can be verified that the estimated SoC converges to the true SoC within 60 s. The statistical results for the US06 tests at different temperatures are provided in Table III. For the temperatures of 15 °C, 25 °C, 35 °C, and 45 °C, the maximum SoC estimation errors are confined to an error margin of 0.02, which is slightly more than that of the FTP75 test that could be attributed to increased fluctuations in the input current profile. During the US06 tests, the terminal voltage profiles at different temperatures are shown in Fig.5(d). Similar to the previous case, despite a variation of 48 mV in the voltage profiles, the variation in the estimated SoC is confined within the order of 10^{-5}. The above simulation studies reveal that the estimated SoC does not substantially change with temperature. However, at very low temperatures of −10 °C and 0 °C, the estimation performance deteriorated with maximum error increasing up to 0.06.

Thus, it can be concluded that the proposed observer performs well for dynamic driving cycles in a wide temperature range of 15 °C–45 °C. In the presence of fluctuating current
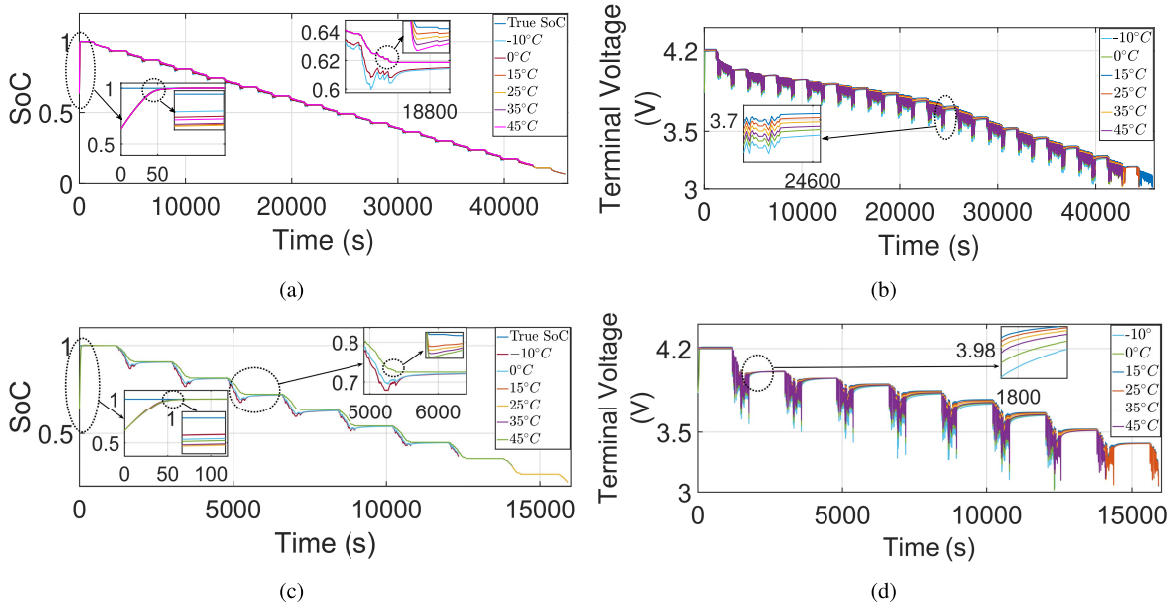
Fig. 5. Plots for (a) SoC estimation and (b) terminal voltages for FTP75 tests at −10 °C, 0 °C, 15 °C, 25 °C, 35 °C, and 45 °C using the measurements from the P2D model. Plots for (c) SoC estimation and (d) terminal voltages for US06 tests at −10 °C, 0 °C, 15 °C, 25 °C, 35 °C, and 45 °C using the measurements from the P2D model.

profile with maximum variation up to 3-C rate, the estimation performance degrades at low temperatures.

Furthermore, US06 tests are carried out at various temperatures in the range of −10 °C–45 °C to evaluate the performance of the observer-based SoC estimation algorithms at high current rates of 5 and 7 C. Fig. 6(a) and (b) illustrates the temporal profile of SoC estimation error for the above tests at various temperatures. It is worth mentioning that the maximum SoC error is limited within 6% in the temperature range of 15 °C–45 °C. However, at low temperatures of −10 °C and 0 °C, the maximum errors are as high as 10%.

The above discussion reveals that the proposed observer is effective in estimating SoC for a wide range of temperatures from 15 °C to 45 °C for high *C*-rate fluctuating current profiles. However, the performance degrades substantially at low temperature −10 °C and 0 °C for higher *C*-rates of 5 and 7 C. At these temperatures, the COSPM should be augmented with an appropriate thermal model of the lithium-ion cell to explicitly deal with the temperature variations.

C. Comparative Analysis

Two cases are considered to assess the SoC estimation results with: 1) the proposed observer and 2) the UKF techniques [3], [36]. The parameters for the observer in (33) applied to the COSPM in (29) were the same as before. The UKF is designed for the COSPM in (25) following the design steps given in [3]. The initial covariance matrix, the process noise covariance matrix, and the measurement covariance are chosen as $[c_1, c_i]$, $c_1 = 10^{-5}$, $c_i = 10^{-3}$, $i = 2, \ldots, 14$, $[pc_1, pc_i]$, $pc_1 = 5 \times 10^{-4}$, $pc_i = 10^{-6}$, $i = 2, \ldots, 14$, and 10^{-10}, respectively. The parameters concerning the unscented transformation are taken as $\alpha = 1$, $\beta = 2$, and $\kappa = 0$ [33]. The design parameters of the UKF-based SoC estimation algorithm for the COSPM are obtained by running extensive numerical
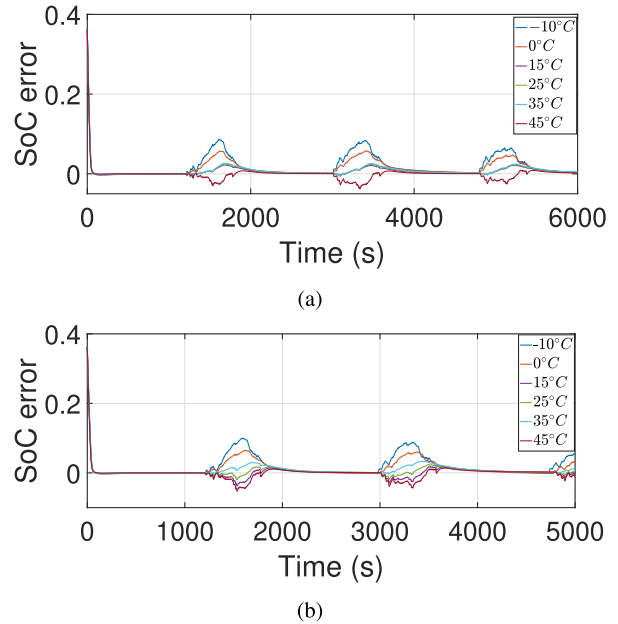

Fig. 6. Plots for SoC estimation error for US06 tests at −10 °C, 0 °C, 15 °C, 25 °C, 35 °C, and 45 °C using the measurements from the P2D model for (a) 5- and (b) 7-C rates.

simulations and are tuned based on trial and error. The readers are advised to refer [3] for further details of the design of the UKF. The SoC estimation results of the proposed observer and the UKF applied to the COSPM are compared with that of true SoC for the US06 test with maximum current fluctuations up to the 3-C rate at 25 °C. When the voltage information of the COSPM is utilized to estimate the SoC, the mean and the maximum values of the SoC estimation error are found to be 4.02×10^{-4} and 5.12×10^{-3}, respectively, for the proposed observer compared to 3.5806×10^{-4} and 4.6×10^{-3}
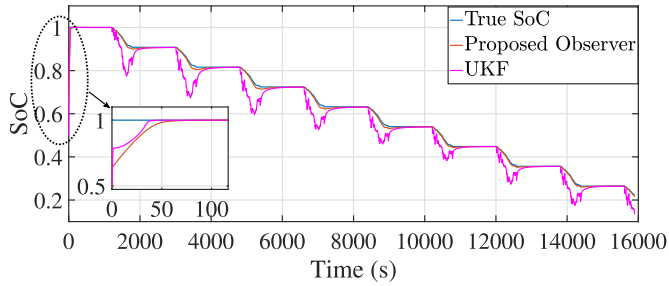
Fig. 7. Comparison of SoC estimated by the proposed observer and the UKF that utilizes the voltage measurements of the P2D model.

for the UKF. The mean and maximum SoC errors for both cases are almost of the same order. Next, the performance of SoC estimation by the observer and the UKF is investigated while utilizing the voltage information of the P2D model for the same test. Fig. 7 illustrates the temporal profile of the estimated SoC using the voltage measurement from the P2D model. A zoomed-in view of the initial portion of the plot shows that the convergence time for all the cases is nearly the same. The maximum SoC estimation error is bounded within the 3% band for the observer, while it reaches up to 20% for the UKF when the current fluctuations are high. The mean error (ME) and ISE for the observer are computed as 3.1×10^{-3} and 2.019, and for the UKF as 3.03×10^{-2} and 6.121, respectively. The above discussion indicates that the proposed observer, when applied to the reduced-order COSPM, provides a more accurate SoC estimate despite a large initial error due to the choice of guess.

D. Robustness Analysis

We now investigate the robustness issues and evaluate the proposed observer's efficacy based on the COSPM in (29) in the presence of bounded uncertainty in the parameters, $R_{s,i}$, $D_{s,i}$, and $D_{e,i}$. In a practical situation, it is difficult to obtain accurate information about the initial SoC of the lithium-ion cell [3]. Hence, the initial SoC guess value is chosen randomly between (0, 1). Monte Carlo simulations with 200 trials were performed at 15 °C, 25 °C, 35 °C, and 45 °C for the US06 dynamic current test.

Remark 3: The temperature-dependent variations in $D_{s,i}$, $D_{e,i}$, and κ_i are obtained using the Arrhenius equation. It is important to note that a lumped uncertainty of $\pm 30\%$ in the elements of the matrices, $\Delta A(t)$ and $\Delta B(t)$ in (29), is considered. The parametric uncertainties can be due to factors, such as measurement uncertainties and modeling inaccuracies. This study considers a ± 10 °C uncertainty in cell temperature, which corresponds to an uncertainty of $\pm 26\%$ in the elements of A for the diffusion coefficient of the positive electrode. With the positive electrode's diffusion coefficient being the most sensitive temperature-dependent parameter, a global $\pm 30\%$ uncertainty is considered for the matrices A and B.

The statistical results of the random numerical simulations for the proposed observer and the UKF are presented in Table IV. It is found that the ME and the ISE for the SoC estimation error with the COSPM-based observer are about ten times lower than that of the UKF at all temperatures. It can

TABLE IV
MEAN VALUES AND STANDARD DEVIATIONS (SDs) OF THE PI ME AND ISE FOR 200 MONTE CARLO SIMULATIONS OF SoC ESTIMATION BY THE PROPOSED OBSERVER AND UKF FOR US06 DYNAMIC TESTS AT -10 °C, 0 °C, 15 °C, 25 °C, 35 °C, AND 45 °C
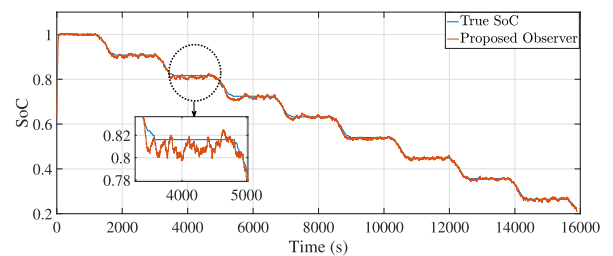
Algorithm	Temperature (°C)	Mean error	ISE
	-10°C	1.09×10^{-3}	3.902
	0°C	8.13×10^{-4}	2.711
COSPM-based observer	15°C	6.78×10^{-4}	1.801
	25°C	6.34×10^{-4}	1.799
	35°C	6.21×10^{-4}	1.792
	45°C	6.32×10^{-4}	1.796
	-10°C	2.75×10^{-3}	11.125
	5°C	1.95×10^{-3}	7.813
UKF	15°C	1.30×10^{-3}	5.889
	25°C	1.28×10^{-3}	5.786
	35°C	1.20×10^{-3}	5.132
	45°C	1.24×10^{-3}	5.200
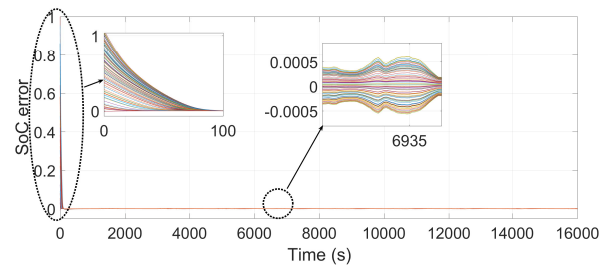
(a)
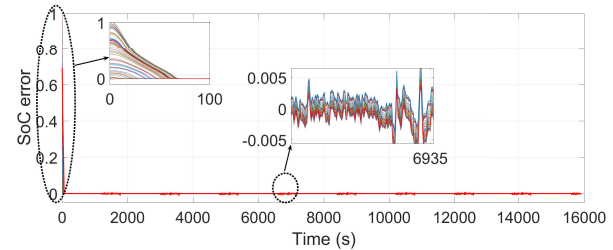
(b)

(c)

Fig. 8. SoC estimation errors of (a) proposed observer and (b) UKF for 200 random Monte Carlo simulations for US06 at 25 °C. (c) Plots for estimated SoC in the presence of measurement noise for the observer utilizing the voltage measurements from the P2D model.

be inferred from Fig. 8(a) and (b) that the maximum values of the SoC estimation error for the proposed observer are at least one order of magnitude smaller than that of the UKF. It is important to note that, for both the observer and the UKF, the voltage from the COSPM is used for the estimation purpose. It can be observed from Fig. 8(c) that the convergence time for both the proposed observer and the UKF is approximately

the same (<70 s). It can be inferred from Table IV that the proposed observer is superior to the UKF in providing more accurate SoC estimates in the presence of large variation in the system parameters and unknown initial conditions. Furthermore, the uncertainty in lithium-ion cells due to temperature difference is also accounted for in the robust framework of the observer design since the proposed observer ensured low values of ME and ISE at different temperatures, as provided in Table IV.

The effect of measurement noise on the SoC estimation by the proposed observer is also studied. Current and voltage measurements utilized in the observer algorithm are assumed to be corrupted with white noise with C/120 and 10-mV variances, respectively. Fig. 8(c) shows that, despite the presence of measurement noise in the current and voltage measurement channels of the P2D model for the US06 test at 25 °C, the observer is still able to provide estimates of the SoC within an absolute error bound of 1×10^{-2}.

V. CONCLUSION

The practical applicability of the existing reduced-order electrochemical model of the lithium-ion cell is limited by their low accuracy in high-current applications. To address this issue, an improved version of the SPM based on a semi-analytical solution is presented that accounts for transport in the positive electrode, negative electrode, and electrolyte. The model's predictions are shown to be significantly closer to that of the high-fidelity P2D model compared to its SPM counterparts [8], [16]. The issue of nonobservability that appears in modeling the combined dynamics of the positive and negative electrodes, and the electrolyte is addressed in this work via the proposed control-oriented model. The retention of diffusion dynamical states for both the electrodes makes the model significantly more accurate than using a simple linear approximation between the surface concentrations of the two electrodes. Since SoC estimation is an integral function of the BMS, it is important to obtain a reliable estimate in the presence of large uncertainties in the lithium-ion cells for applications where high current fluctuations can be anticipated. Based on the proposed model, a nonlinear observer was proposed in a robust LMI framework with guaranteed convergence of the SoC estimate to its actual value despite large modeling uncertainties. The observer feedback parameters' optimal values were derived by solving a convex optimization problem with LMI constraints. The estimation results of the proposed observer for the dynamic tests with high current fluctuations performed at several temperatures validated its effectiveness in SoC estimation. The problems that arise in dynamic tests at high C-rates when using empirical models, such as ECM and SPM, were circumvented. Furthermore, in-depth robustness analysis for large temperature-induced parametric variability, modeling inaccuracies, and measurement noise was carried out using Monte Carlo simulations. The SoC estimation results with the proposed technique were found to be superior to the existing UKF-based SoC estimation algorithms, especially under high current fluctuation. In summary, the presented work provides a unified framework incorporating the blend of physics and estimation theory for robust model-based SoC

estimation. Future work is directed toward the cell's SoH and internal temperature estimation by incorporating the proposed physics-based model's framework along with thermal and degradation models.

APPENDIX A
PROOF OF THEOREM 1

Consider a positive definite storage function

$$V(\mathbf{e}_o(t)) := \mathbf{e}_o(t)^T \mathbf{P} \mathbf{e}_o(t) \tag{47}$$

where $\mathbf{P} = \mathbf{P}^T > 0$. Differentiating on both sides with respect to time yields

$$\dot{V}(\mathbf{e}_o(t)) = 2\mathbf{e}_o^\mathsf{T}(t)\mathbf{P}\dot{\mathbf{e}}_o(t). \tag{48}$$

Substituting (35) in (48) and expressing it in the quadratic form, one can get

$$\dot{V}(\mathbf{e}_o(t)) = \mathbf{e}_o^T\big[(\mathbf{A} - \mathbf{LK}_{\min})^T\mathbf{P} + \mathbf{P}(\mathbf{A} - \mathbf{LK}_{\min})\big]\mathbf{e}_o \\ - 2\mathbf{e}_o^T\mathbf{PL}\phi(\mathbf{x}, \hat{\mathbf{x}}, u) + 2\mathbf{e}_o^T\mathbf{P}(\Delta\mathbf{A}\mathbf{x} + \Delta\mathbf{B}u) \\ - 2\mathbf{e}_o^T\mathbf{PL}\xi_y. \tag{49}$$

Let us introduce a new variable that contains the uncertain terms in (49) as

$$\xi \triangleq \Delta\mathbf{A}\mathbf{x} + \Delta\mathbf{B}u. \tag{50}$$

Furthermore, (49) can be modified as

$$\dot{V}(\mathbf{e}_o(t)) = \mathbf{z}^T\mathbf{W}_1\mathbf{z} \tag{51}$$

where

$$\mathbf{z} = \big[\,\mathbf{e}_o \;\; \phi(\mathbf{x}, \hat{\mathbf{x}}, u) \;\; \xi \;\; \xi_\mathbf{y}\,\big]^T$$

$$\mathbf{W}_1 = \begin{bmatrix} \Lambda_1 & -\mathbf{PL} & \mathbf{P} & -\mathbf{PL} \\ * & \mathbf{0} & \mathbf{0} & \mathbf{0} \\ * & * & \mathbf{0} & \mathbf{0} \\ * & * & * & \mathbf{0} \end{bmatrix}$$

and $\Lambda_1 = (\mathbf{A} - \mathbf{LK}_{\min})^T\mathbf{P} + \mathbf{P}(\mathbf{A} - \mathbf{LK}_{\min})$. Now, adding and subtracting $\varepsilon_1\|\phi(\mathbf{x}, \hat{\mathbf{x}}, u)\|^2$, $\varepsilon_2\|\xi\|^2$, $\varepsilon_3\|\xi_\mathbf{y}\|^2$ and $\alpha V(\mathbf{e}_o)$ on the right-hand side of (51), one can obtain

$$\dot{V}(\mathbf{e}_o(t)) = \mathbf{z}^T\mathbf{W}_2\mathbf{z} - \alpha V(\mathbf{e}_o) + \varepsilon_1\|\phi(\mathbf{x}, \hat{\mathbf{x}}, u)\|^2 + \varepsilon_2\|\xi\|^2 \\ + \varepsilon_3\|\xi_\mathbf{y}\|^2$$

$$\mathbf{W}_2 = \begin{bmatrix} \Lambda_2 & -\mathbf{PL} & \mathbf{P} & -\mathbf{PL} \\ * & -\varepsilon_1\mathbf{I}_{n\times n} & \mathbf{0} & \mathbf{0} \\ * & * & -\varepsilon_2\mathbf{I}_{n\times n} & \mathbf{0} \\ * & * & * & -\varepsilon_3\mathbf{I}_{n\times n} \end{bmatrix} \tag{52}$$

and $\Lambda_2 = (\mathbf{A} - \mathbf{LK}_{\min})^T\mathbf{P} + \mathbf{P}(\mathbf{A} - \mathbf{LK}_{\min}) + \alpha\mathbf{P}$. From Assumptions 2 and 3, (52) can be modified further as

$$\dot{V}(\mathbf{e}_o(t)) = \mathbf{z}^T\mathbf{W}_3\mathbf{z} - \alpha V(\mathbf{e}_o(t)) + \varepsilon_2\|\xi\|^2 + +\varepsilon_3\|\xi_\mathbf{y}\|^2 \tag{53}$$

where

$$\mathbf{W}_3 = \begin{bmatrix} \Lambda_3 & -\mathbf{PL} & \mathbf{P} & -\mathbf{PL} \\ * & -\varepsilon_1\mathbf{I}_{n\times n} & \mathbf{0} & \mathbf{0} \\ * & * & -\varepsilon_2\mathbf{I}_{n\times n} & \mathbf{0} \\ * & * & * & -\varepsilon_3\mathbf{I}_{n\times n} \end{bmatrix}$$

$$\mathbf{B}_p = \left[\begin{array}{ccc} \frac{2}{R_{s,p}a_{s,p}FL_p} & \frac{2}{R_{s,p}a_{s,p}FL_p} & \frac{2}{R_{s,p}a_{s,p}FL_p} \end{array} \right]^T \in \mathbb{R}^{3\times 1} \tag{61}$$

$$\mathbf{M}_e = \begin{bmatrix} -\left[\frac{2}{3} + \left(\frac{\epsilon_{e,n}}{\epsilon_{e,s}}\right)^{\mathrm{brug}}\frac{L_s}{L_n}\right] & -\left[\frac{1}{3} + \left(\frac{\epsilon_{e,p}}{\epsilon_{e,s}}\right)^{\mathrm{brug}}\frac{L_s}{2L_p}\right] \\ -\left[\frac{2}{3} + \left(\frac{\epsilon_{e,n}}{\epsilon_{e,s}}\right)^{\mathrm{brug}}\frac{2L_s}{3L_n}\right] & -\left(\frac{\epsilon_{e,p}}{\epsilon_{e,s}}\right)^{\mathrm{brug}}\frac{L_s}{6L_p} \end{bmatrix} \in \mathbb{R}^{2\times 2} \tag{62}$$

$$\mathbf{A}_e = \begin{bmatrix} \frac{2D_{e,n}}{\epsilon_{e,n}L_n^2} & \frac{D_{e,p}}{\epsilon_{e,p}L_p^2} \\ \frac{2D_{e,n}}{\epsilon_{e,n}L_n^2} + \frac{2D_{e,s}}{\epsilon_{e,s}L_s^2}\left(\frac{\epsilon_{e,n}}{\epsilon_{e,s}}\right)^{\mathrm{brug}}\frac{L_s}{L_n} & -\frac{D_{e,s}}{\epsilon_{e,s}L_s^2}\left(\frac{\epsilon_{e,p}}{\epsilon_{e,s}}\right)^{\mathrm{brug}}\frac{L_s}{L_p} \end{bmatrix} \in \mathbb{R}^{2\times 2} \tag{63}$$

$$\mathbf{B}_e = \left[\begin{array}{cc} \frac{(1-t_+^0)}{FC_{0,e}}\left[\frac{1}{L_n\epsilon_{e,n}} + \frac{1}{L_p\epsilon_{e,p}}\right] & \frac{(1-t_+^0)}{FC_{0,e}}\frac{1}{L_n\epsilon_{e,n}} \end{array} \right]^T \in \mathbb{R}^{2\times 1} \tag{64}$$

and $\Lambda_3 = (\mathbf{A} - \mathbf{L}\mathbf{K}_{\min})^T\mathbf{P} + \mathbf{P}(\mathbf{A} - \mathbf{L}\mathbf{K}_{\min}) + \alpha\mathbf{P} + \varepsilon_1(L_h + \mathbf{K}_{\min})\mathbf{I}_{n\times n}$. Using the bounds mentioned in (39) and (40) in Assumptions 3 and 4, $\dot{V}(\mathbf{e}_o)$ in (53) can be expressed as

$$\dot{V}(\mathbf{e}_o(t)) \le \mathbf{z}^T\mathbf{W}_3\mathbf{z} - \alpha V(\mathbf{e}_o(t)) + c \tag{54}$$

where $c = \varepsilon_2(\delta_a^2 X_+^2 + \delta_b^2 U_+^2) + \varepsilon_3\mathcal{Y}_+^2$. If the following matrix inequality is satisfied

$$\mathbf{W}_3 < \mathbf{0} \tag{55}$$

then the time derivative of the Lyapunov function in (54) can be expressed as

$$\dot{V}(t) \le -\alpha V(t) + c. \tag{56}$$

Solving (56) and taking the limit, one can substitute the expression for $V(\mathbf{e}_o)$ from (47) and obtain

$$\limsup_{t\to\infty} \mathbf{e}_o^T\mathbf{P}\mathbf{e}_o \le \frac{c}{\alpha} \implies \limsup_{t\to\infty} \mathbf{e}_o^T[\mathbf{P}_{\mathrm{attr}}]\mathbf{e}_o \le 1 \tag{57}$$

where $\mathbf{P}_{\mathrm{attr}} = (\alpha/c)\mathbf{P}$. Hence, the trajectories of the estimation error $\mathbf{e}_o(t)$ exponentially converge to the convex set as $t \to \infty$. This proves the theorem.

APPENDIX B
STATE-SPACE DESCRIPTION OF THE PROPOSED COSPM

The different matrices involved in the state-space representation of the proposed model in (25) are given as

$$\mathbf{A}_n = \mathrm{diag}\left(0, \frac{\lambda_1^2, D_{s,n}}{R_{s,n}^2}, \frac{\lambda_2^2, D_{s,n}}{R_{s,n}^2}, \dots, \frac{\lambda_9^2, D_{s,n}}{R_{s,n}^2}\right) \in \mathbb{R}^{10\times 10} \tag{58}$$

where $\mathrm{diag}(a, b, \dots)$ denotes the diagonal matrix with elements $a, b, \dots$

$$\mathbf{B}_n = [-3/A_1 - 2/A_1, \dots, -2/A_1]^T \in \mathbb{R}^{10\times 1} \tag{59}$$

where $A_1 = R_{s,n}a_{s,n}FL_n$

$$\mathbf{A}_p = \mathrm{diag}\left(\lambda_1^2 A_2, \lambda_2^2 A_2, \lambda_3^2 A_2\right) \in \mathbb{R}^{3\times 3} \tag{60}$$

where $A_2 = D_{s,p}/R_{s,p}^2$. (61)–(64), as shown at the top of the page, and the nonlinear output equation in (30) for the cell voltage is given by

$$\begin{aligned} y = h(x, u) = {} & \frac{RT}{\alpha_a F}\sinh^{-1}\left[\frac{I}{a_{s,p}FL_p j_{0,p}(\bar{C}_{s,p})}\right] \\ & - \frac{RT}{\alpha_a F}\sinh^{-1}\left[-\frac{I}{a_{s,n}FL_n j_{0,n}(\bar{C}_{s,n})}\right] + U_p(\bar{C}_{s,p}) \\ & - U_n(\bar{C}_{s,n}) - \frac{RT(t_+^0 - 1)}{F} \\ & \times \left[\frac{2(a_{n,1} + 2a_{n,2})}{3(a_{n,0} + a_{n,1} + a_{n,2})} + \frac{(a_{s,1} + 2a_{s,2})}{(a_{s,0} + a_{s,1} + a_{s,2})}\right. \\ & \left. + \frac{a_{s,1}}{a_{s,0}} + \frac{2a_{p,1}}{3a_{p,0}}\right] \\ & \times \left[\frac{L_p}{3\kappa_p^{\mathrm{eff}}} + \frac{L_s}{\kappa_s^{\mathrm{eff}}} + \frac{L_n}{3\kappa_n^{\mathrm{eff}}} + \frac{L_p}{3\sigma_p^{\mathrm{eff}}} + \frac{L_n}{3\sigma_n^{\mathrm{eff}}}\right]u. \end{aligned} \tag{65}$$

REFERENCES

[1] N. A. Chaturvedi, R. Klein, J. Christensen, J. Ahmed, and A. Kojic, "Algorithms for advanced battery-management systems," *IEEE Control Syst. Mag.*, vol. 30, no. 3, pp. 49–68, Jun. 2010.

[2] A. Nath, R. Gupta, R. Mehta, S. S. Bahga, A. Gupta, and S. Bhasin, "Attractive ellipsoid sliding mode observer design for state of charge estimation of lithium-ion cells," *IEEE Trans. Veh. Technol.*, vol. 69, no. 12, pp. 14701–14712, Dec. 2020.

[3] G. L. Plett, *Battery Management Systems: Equivalent-Circuit Methods*, vol. 2. Norwood, MA, USA: Artech House, 2015.

[4] S. Zhang, X. Guo, X. Dou, and X. Zhang, "A rapid online calculation method for state of health of lithium-ion battery based on Coulomb counting method and differential voltage analysis," *J. Power Sources*, vol. 479, Dec. 2020, Art. no. 228740.

[5] X. Shu, G. Li, J. Shen, W. Yan, Z. Chen, and Y. Liu, "An adaptive fusion estimation algorithm for state of charge of lithium-ion batteries considering wide operating temperature and degradation," *J. Power Sources*, vol. 462, Jun. 2020, Art. no. 228132.

[6] M. Rashid and A. Gupta, "Experimental assessment and model development of cycling behavior in Li-ion coin cells," *Electrochim. Acta*, vol. 231, pp. 171–184, Mar. 2017.

[7] A. Jokar, B. Rajabloo, M. Désilets, and M. Lacroix, "Review of simplified pseudo-two-dimensional models of lithium-ion batteries," *J. Power Sources*, vol. 327, pp. 44–55, Jul. 2016.

[8] G. Ning and B. N. Popov, "Cycle life modeling of lithium-ion batteries," *J. Electrochem. Soc.*, vol. 151, no. 10, 2004, Art. no. A1584.

[9] G. Richardson, I. Korotkin, R. Ranom, M. Castle, and J. M. Foster, "Generalised single particle models for high-rate operation of graded lithium-ion electrodes: Systematic derivation and validation," *Electrochim. Acta*, vol. 339, Apr. 2020, Art. no. 135862.

[10] S. Dey, B. Ayalew, and P. Pisu, "Nonlinear robust observers for state-of-charge estimation of lithium-ion cells based on a reduced electrochemical model," *IEEE Trans. Control Syst. Technol.*, vol. 23, no. 5, pp. 1935–1942, Sep. 2015.

[11] R. Gu, P. Malysz, H. Yang, and A. Emadi, "On the suitability of electrochemical-based modeling for lithium-ion batteries," *IEEE Trans. Transport. Electrific.*, vol. 2, no. 4, pp. 417–431, Dec. 2016.

[12] D. Zhang, S. Dey, L. D. Couto, and S. J. Moura, "Battery adaptive observer for a single-particle model with intercalation-induced stress," *IEEE Trans. Control Syst. Technol.*, vol. 28, no. 4, pp. 1363–1373, 2020.

[13] R. Mehta and A. Gupta, "An improved single-particle model with electrolyte dynamics for high current applications of lithium-ion cells," *Electrochim. Acta*, vol. 389, Sep. 2021, Art. no. 138623.

[14] R. Romagnoli, L. D. Couto, A. Goldar, M. Kinnaert, and E. Garone, "A feedback charge strategy for Li-ion battery cells based on reference governor," *J. Process Control*, vol. 83, pp. 164–176, Nov. 2019.

[15] L. D. Couto and M. Kinnaert, "Internal and sensor fault detection and isolation for Li-ion batteries," *IFAC-PapersOnLine*, vol. 51, no. 24, pp. 1431–1438, 2018.

[16] E. Prada, D. Di Domenico, Y. Creff, J. Bernard, V. Sauvant-Moynot, and F. Huet, "Simplified electrochemical and thermal model of LiFePO$_4$-graphite Li-ion batteries for fast charge applications," *J. Electrochem. Soc.*, vol. 159, no. 9, pp. A1508–A1519, 2012.

[17] B. Liu, X. Tang, and F. Gao, "Joint estimation of battery state-of-charge and state-of-health based on a simplified pseudo-two-dimensional model," *Electrochim. Acta*, vol. 344, Jun. 2020, Art. no. 136098.

[18] R. Xiong, L. Li, and Q. Yu, "Improved single particle model based state of charge and capacity monitoring of lithium-ion batteries," in *Proc. IEEE 89th Veh. Technol. Conf. (VTC-Spring)*, Apr. 2019, pp. 1–5.

[19] X. Lin, X. Hao, Z. Liu, and W. Jia, "Health conscious fast charging of Li-ion batteries via a single particle model with aging mechanisms," *J. Power Sources*, vol. 400, pp. 305–316, Oct. 2018.

[20] S. J. Moura, F. B. Argomedo, R. Klein, A. Mirtabatabaei, and M. Krstic, "Battery state estimation for a single particle model with electrolyte dynamics," *IEEE Trans. Control Syst. Technol.*, vol. 25, no. 2, pp. 453–468, Mar. 2017.

[21] J. Li, R. G. Landers, and J. Park, "A comprehensive single-particle-degradation model for battery state-of-health prediction," *J. Power Sources*, vol. 456, Apr. 2020, Art. no. 227950.

[22] N. Lotfi, J. Li, R. G. Landers, and J. Park, "Li-ion battery state of health estimation based on an improved single particle model," in *Proc. Amer. Control Conf. (ACC)*, May 2017, pp. 86–91.

[23] D. Di Domenico, A. Stefanopoulou, and G. Fiengo, "Lithium-ion battery state of charge and critical surface charge estimation using an electrochemical model-based extended Kalman filter," *J. Dyn. Syst., Meas., Control*, vol. 132, no. 6, Nov. 2010, Art. no. 48109.

[24] X. Han, M. Ouyang, L. Lu, and J. Li, "Simplification of physics-based electrochemical model for lithium ion battery on electric vehicle—Part I: Diffusion simplification and single particle model," *J. Power Sources*, vol. 278, pp. 802–813, Mar. 2015.

[25] Y. Hu, Y. Yin, Y. Bi, and S.-Y. Choe, "A control oriented reduced order electrochemical model considering variable diffusivity of lithium ions in solid," *J. Power Sources*, vol. 468, Aug. 2020, Art. no. 228322.

[26] D. W. Limoge and A. M. Annaswamy, "An adaptive observer design for real-time parameter estimation in lithium-ion batteries," *IEEE Trans. Control Syst. Technol.*, vol. 28, no. 2, pp. 505–520, Mar. 2020.

[27] B. Jenkins, A. Krupadanam, and A. M. Annaswamy, "Fast adaptive observers for battery management systems," *IEEE Trans. Control Syst. Technol.*, vol. 28, no. 3, pp. 776–789, May 2020.

[28] N. Lotfi, R. G. Landers, J. Li, and J. Park, "Reduced-order electrochemical model-based SOC observer with output model uncertainty estimation," *IEEE Trans. Control Syst. Technol.*, vol. 25, no. 4, pp. 1217–1230, Jun. 2017.

[29] M. Guo and R. E. White, "An approximate solution for solid-phase diffusion in a spherical particle in physics-based Li-ion cell models," *J. Power Sources*, vol. 198, pp. 322–328, Jan. 2012.

[30] A. Allam and S. Onori, "An interconnected observer for concurrent estimation of bulk and surface concentration in the cathode and anode of a lithium-ion battery," *IEEE Trans. Ind. Electron.*, vol. 65, no. 9, pp. 7311–7321, Sep. 2018.

[31] S. Dey and B. Ayalew, "Real-time estimation of lithium-ion concentration in both electrodes of a lithium-ion battery cell utilizing electrochemical–thermal coupling," *J. Dyn. Syst., Meas., Control*, vol. 139, no. 3, Mar. 2017, Art. no. 031007.

[32] Z. Cen and P. Kubiak, "Lithium-ion battery SOC/SOH adaptive estimation via simplified single particle model," *Int. J. Energy Res.*, vol. 44, no. 15, pp. 12444–12459, Dec. 2020.

[33] G. L. Plett, "Extended Kalman filtering for battery management systems of LiPB-based HEV battery packs: Part 3. State and parameter estimation," *J. Power Sources*, vol. 134, no. 2, pp. 277–292, 2004.

[34] Y. Li, J. Chen, and F. Lan, "Enhanced online model identification and state of charge estimation for lithium-ion battery under noise corrupted measurements by bias compensation recursive least squares," *J. Power Sources*, vol. 456, Apr. 2020, Art. no. 227984.

[35] S. Afshar, K. Morris, and A. Khajepour, "State-of-charge estimation using an EKF-based adaptive observer," *IEEE Trans. Control Syst. Technol.*, vol. 27, no. 5, pp. 1907–1923, Sep. 2019.

[36] G. L. Plett, "Sigma-point Kalman filtering for battery management systems of LiPB-based HEV battery packs: Part 2: Simultaneous state and parameter estimation," *J. Power Sources*, vol. 161, pp. 1369–1384, Oct. 2006.

[37] W. Li *et al.*, "Electrochemical model-based state estimation for lithium-ion batteries with adaptive unscented Kalman filter," *J. Power Sources*, vol. 476, Nov. 2020, Art. no. 228534.

[38] Y. Wang, C. Zhang, and Z. Chen, "A method for state-of-charge estimation of LiFePO4 batteries at dynamic currents and temperatures using particle filter," *J. Power Sources*, vol. 279, pp. 306–311, Apr. 2015.

[39] A. Pozzi, M. Zambelli, A. Ferrara, and D. M. Raimondo, "Balancing-aware charging strategy for series-connected lithium-ion cells: A nonlinear model predictive control approach," *IEEE Trans. Control Syst. Technol.*, vol. 28, no. 5, pp. 1862–1877, Sep. 2020.

[40] Q. Zhu, L. Li, X. Hu, N. Xiong, and G.-D. Hu, "H$_\infty$-based nonlinear observer design for state of charge estimation of lithium-ion battery with polynomial parameters," *IEEE Trans. Veh. Technol.*, vol. 66, no. 12, pp. 10853–10865, Dec. 2017.

[41] J. Du, Z. Liu, Y. Wang, and C. Wen, "An adaptive sliding mode observer for lithium-ion battery state of charge and state of health estimation in electric vehicles," *Control Eng. Pract.*, vol. 54, pp. 81–90, Sep. 2016.

[42] Y. Shtessel, C. Edwards, L. Fridman, and A. Levant, *Sliding Mode Control and Observation*. New York, NY, USA: Springer, 2014.

[43] B. Ning, B. Cao, B. Wang, and Z. Zou, "Adaptive sliding mode observers for lithium-ion battery state estimation based on parameters identified online," *Energy*, vol. 153, pp. 732–742, Jun. 2018.

[44] A. Nath, D. Deb, and R. Dey, "Robust observer-based adaptive control of blood glucose in diabetic patients," *Int. J. Control*, vol. 94, no. 11, pp. 3054–3067, 2020.

[45] R. Falcon, H. Rios, M. Mera, and A. Dzul, "Attractive ellipsoid-based robust control for quadrotor tracking," *IEEE Trans. Ind. Electron.*, vol. 67, no. 9, pp. 7851–7860, Sep. 2020.

[46] W.-B. Gu and C.-Y. Wang, "Thermal and electrochemical coupled modeling of a lithium-ion cell," *Proc. Electrochem. Soc.*, vol. 99, no. 1, pp. 748–762, 2000.

[47] M. Doyle, J. Newman, A. S. Gozdz, C. N. Schmutz, and J. M. Tarascon, "Comparison of modeling predictions with experimental data from plastic lithium ion cells," *J. Electrochemical Soc.*, vol. 143, no. 6, p. 1890, 1996.

[48] H. Wang and R. Rajamani, "Electromagnetic position estimation using active current control and nonlinear observer," in *Proc. Amer. Control Conf. (ACC)*, Jul. 2020, pp. 1347–1352.

[49] K. Kumaresan, G. Sikha, and R. E. White, "Thermal model for a Li-ion cell," *J. Electrochem. Soc.*, vol. 155, no. 2, 2008, Art. no. A164.

[50] S. Tang, L. Camachosolorio, Y. Wang, and M. Krsti, "State-of-charge estimation from a thermal–electrochemical model of lithium-ion batteries," *Automatica*, vol. 83, pp. 206–219, Sep. 2017.

[51] P. Blondel, R. Postoyan, S. Rael, S. Benjamin, and P. Desprez, "Nonlinear circle-criterion observer design for an electrochemical battery model," *IEEE Trans. Control Syst. Technol.*, vol. 27, no. 2, pp. 889–897, Mar. 2019.